https://doi.org/10.5194/egusphere-2026-5310
Preprint. Discussion started: 9 September 2026

Wind Profile Retrieval Using Ensemble Learning and Mobile Brightness Temperature over the Tibetan Plateau

Yingli MA[1], Xinghong CHENG[1], Jiajia MAO[2], Guirong XU[3], Nan LI[1], and Bing CHEN[4]

[1]State Key Laboratory of Severe Weather Meteorological Science and Technology (LaSW), Chinese Academy of Meteorological Sciences, Beijing 100081, China.
[2]Meteorological Observation Center, China Meteorological Administration, Beijing 100081, China
[3]Hubei Key Laboratory for Heavy Rain Monitoring and Warning Research, Institute of Heavy Rain, China Meteorological Administration, Wuhan 430205, China
[4]Heavy Rain and Drought-Flood Disasters in Plateau and Basin Key Laboratory of Sichuan Province, Institute of Tibetan Plateau Meteorology, China Meteorological Administration, Chengdu 610213, China.

Correspondence to: Xinghong Cheng (cxingh@cma.gov.cn) and Jiajia Mao (maojj@cma.gov.cn)

Abstract. Sparse and infrequent upper-air observations over the Three-River Source Region (TRSR) of the Tibetan Plateau (TP) severely limit the capability for extensive and continuous wind profile (WP) monitoring. A WP retrieval model was developed via ensemble learning (XGBoost+CatBoost), trained on TB data from 14 fixed-site ground-based microwave radiometers (GMWR) and WP radiosonde observations (Raob), and then applied to mobile GMWR observations over the TRSR. After strict QC of TB data, three distribution-alignment methods (Quantile Transformer, PCA Whitening, RankGauss) were used to mitigate the TB discrepancy between fixed and mobile GMWR. A nonlinear weighted regression loss function was introduced to reduce the central tendency effect in long-tailed wind-speed distributions. Retrieved WP from 14 fixed-site GMWR test data agreed well with Raob (R = 0.96, RMSE = 2.24 $m\ s^{-1}$, MAE = 1.57 $m\ s^{-1}$). Retrieval errors in the 600–700 hPa layer were lower at 08:00 BT than at 20:00, and smaller in lower-altitude regions. Mobile GMWR retrievals reproduced WP variability with mean biases below 2 $m\ s^{-1}$ relative to Raob, though errors increased for upper-level strong winds and at high altitudes; against Raob-corrected ERA5, the RMSE and MAE were 2.66 and 2.25 $m\ s^{-1}$, respectively. This study offers a novel pathway to optimize ground-based vertical remote sensing, enhance meteorological support for the low-altitude economy, and improve wind energy assessment and forecasting.

1 Introduction

Wind profiles are critical for both understanding boundary-layer dynamics, weather systems, and moisture/energy cycles, and for practical applications in aviation, wind energy, and severe weather monitoring (Van Zandt, 2000; Liu et al., 2020; Xia et al., 2024). The Three-River Source Region (TRSR) of the Tibetan Plateau (TP) has a mean elevation over 4,000 m and complex terrain, where wind fields are strongly influenced by plateau heating, mountain–valley circulations, and local turbulence (Yang et al., 2023; Li et al., 2021). As a key component of the "Asian Water Tower" and "Third Pole," the TP also strongly influences the East Asian monsoon, water cycle, and regional climate (Li et al., 2021; Kuang and Jiao, 2016).

https://doi.org/10.5194/egusphere-2026-5310
Preprint. Discussion started: 9 September 2026

Continuous wind profile monitoring is therefore important for understanding plateau atmospheric dynamics and improving weather forecasting and numerical modeling. Wind profiles are observed with radiosondes, wind profiler radars, Doppler wind lidars, and aircraft, among which radiosondes provide accurate vertical wind measurements but are limited by sparse coverage, low frequency, and balloon drift (WMO, 2021; Liu et al., 2025). Ground-based microwave radiometers (GMWR) provide continuous, all-weather brightness temperature observations at 22–30 and 51–59 GHz and retrieve high-temporal-resolution atmospheric thermodynamic profiles, serving as an important complement to radiosondes (Hogg et al., 1983; Westwater, 1993). GMWR observations over the TP have been applied to land-surface processes (Su et al., 2020; Wen et al., 2021), surface freeze–thaw (Xi et al., 2020), atmospheric thermodynamics and cloud water (Huang et al., 2001; Liu et al., 2015; Xu et al., 2019), temperature inversions at Mount Qomolangma (Zhao et al., 2024), summer nonprecipitating cloud properties (Xu et al., 2024), and tropospheric thermal and moisture variations (Chen et al., 2024). Most previous studies rely on fixed-site GMWR observations with limited spatial coverage. Mobile GMWR on vehicles, ships, and aircraft have therefore been explored to extend atmospheric profiling over larger areas (Chen et al., 1996; Karan and Knupp, 2006; Wang et al., 2018; Walbröl et al., 2022; Lei et al., 2023). However, applications over the TP remain limited. Cheng et al. (2024) conducted the first Mobile Field Observation Campaign of Atmospheric Profiles (MFOCAP) over the TRSR during 17–31 July 2021 and demonstrated the feasibility of continuous, high-spatiotemporal-resolution mobile observations with vehicle-based GMWR over complex terrain.

Beyond thermodynamic information, TB observations with GMWR also contain atmospheric dynamical signatures. Following the physical principles for satellite-based wind profile (WP) retrieval (Velden et al., 2005; Ma et al., 2021), several studies (Chen et al., 2024; Jiang et al., 2026) have developed AI-based methods for WP retrieval from GMWR observations, using ERA5 U/V winds and AI algorithms including LSTM, RNN, and MLP. The retrieval principle involves two components: K-band TBs capture water vapor mass motion, whereas V-band TBs exploit thermodynamic information for WP retrieval via the thermal wind relationship. Specifically, by combining the horizontal temperature distribution across multiple levels with the thermal wind relationship, the vertical shear of the geostrophic wind is derived layer by layer; the WP is then retrieved once the wind speed (WS) at a reference level is known (Velden et al., 2005). Machine learning can further capture nonlinear relationships between TB observations and WP. Neural networks have been used for ocean surface wind retrieval (Stogryn et al., 1994), four-dimensional wind retrieval from satellite radiances (Ma et al., 2021), and GMWR-based WP retrieval with LSTM/RNN/MLP (Chen et al., 2024; Jiang et al., 2026). However, most previous studies used a single-model approach, which may be sensitive to model architecture and training data. Ensemble learning reduces individual-model bias while improving stability and generalization. It has been applied to numerical weather prediction error correction, WS forecasting, and remote-sensing retrieval (Zeng et al., 2024; Deng et al., 2025). XGBoost and CatBoost are particularly advantageous for small-to-medium datasets, combining nonlinear fitting with robustness to overfitting (Chen and Guestrin, 2016; Prokhorenkova et al., 2018).

Previous GMWR WP retrieval over the TP relied mainly on ERA5 winds for model training (Chen et al., 2024), while ERA5 winds may be uncertain over complex terrain (Minola et al., 2024; Ou et al., 2023). Although radiosonde stations are

https://doi.org/10.5194/egusphere-2026-5310
Preprint. Discussion started: 9 September 2026

sparse and low frequency over the TP, they can provide reliable training data. Furthermore, previous studies neglected distribution differences between training and testing samples, as well as the central tendency of long-tailed wind-speed distributions. To address these limitations, TB observations from 14 fixed-site GMWR and mobile GMWR observations over the TP, together with concurrent Raob WP, were used to develop an XGBoost–CatBoost ensemble learning WP retrieval model. Distribution alignment and a wind-speed-weighted regression loss were introduced, and the effects of weather conditions, diurnal TB variations and station elevation were examined. The model was further applied to mobile GMWR observations to assess its applicability and generalization, offering a new pathway for continuous large-area WP retrieval and improved ground-based vertical remote sensing over the TP.

Following this introduction, Section 2 describes the data used in this study. Section 3 details the data processing procedures. The wind profile retrieval approach is presented in Section 4. Section 5 evaluates the retrieval performance for fixed and mobile GMWR observations and discusses the factors affecting retrieval accuracy. Conclusions and discussion are given in Section 6.

2. Data

2.1 GMWR Observations over the TP

TB observations from 14 fixed-site GMWR over the central-eastern TP and surrounding areas were used to construct the WP retrieval model. The sites span Qinghai, Tibet, and Sichuan, with elevations ranging from 342 m (Yibin) to 4533 m (Tuotuohe), and cover the plateau interior, marginal transition zones, and eastern hilly areas (Fig. 1). Site information is listed in Table 1.

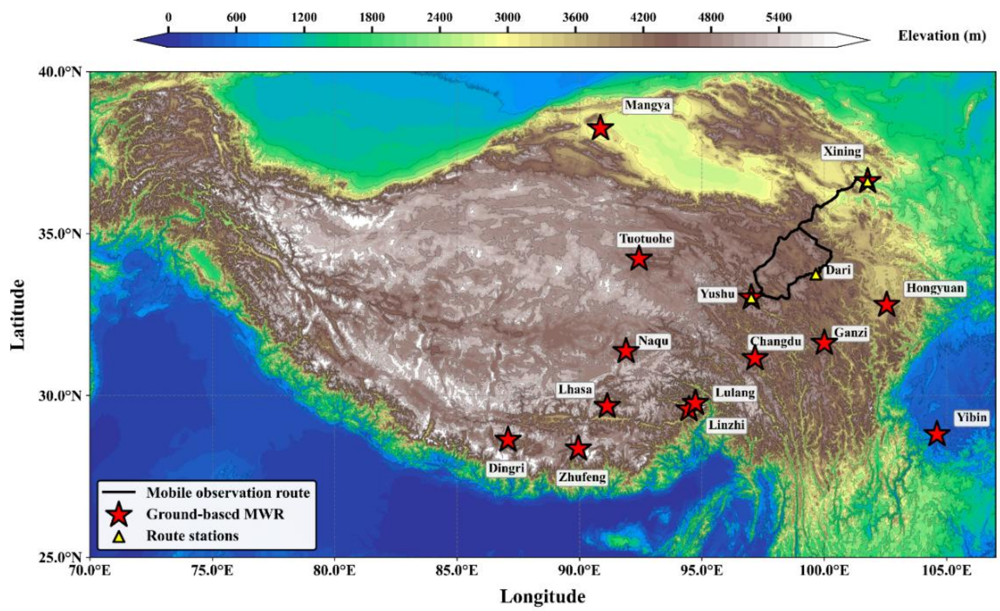

https://doi.org/10.5194/egusphere-2026-5310
Preprint. Discussion started: 9 September 2026

Figure 1: Locations of the 14 fixed-site GMWR and the mobile GMWR observation route over the TP and its surrounding areas.

Multiple GMWR models were deployed at the observation sites, providing continuous multichannel TB observations at 22–58 GHz. Because of slight differences in channel center frequencies among GMWR, 12 common channels (22.240, 23.040, 23.840, 26.240, 27.840, 51.260, 52.280, 53.860, 54.940, 56.660, 57.300, and 58.000 GHz) were selected as inputs for the WP retrieval model. The raw TB data were quality-controlled to remove missing and anomalous values, then collocated with WP observations from nearby radiosonde stations, yielding 14,020 valid samples for training, validation, and testing.

Table 1: Basic information on the 14 fixed-site GMWR over the Tibetan Plateau and sample statistics before and after TB quality control.

Instrument model, manufacturer	Region	Station	Elevation (m)	Observation period	Sample number before QC	Sample number after QC
TK001, Shanghai Leitan Technology Co., Ltd	Qinghai	Xining	2295	2024/8/23-2026/1/28	1040	696
		Yushu	3681	2024/9/12-2025/8/20	679	560
		Tuotuohe	4533	2025/10/25-2026/1/28	187	163
MWP967KV, Xi'an Electronic Engineering Research Institute		Mangya	2945	2021/1/1-2021/12/31 2023/5/1-2026/4/29	2692	2541
HTG4, Beijing Airda Electronic Equipment Co., Ltd.	Tibet	Lhasa	3649	2025/5/30-2026/1/1	423	363
		Changdu	3306	2023/1/1-2026/1/1	2161	1653
		Dingri	4300	2023/1/1-2026/1/1	2081	1870
		Linzhi	2991	2023/1/1-2026/1/1	2173	1529
MWP967KV, Xi'an Electronic Engineering Research Institute		Changdu	3306	2021/6/1-2021/8/31	118	61
		QOMS	4294	2021/6/1-2021/8/31	127	93

https://doi.org/10.5194/egusphere-2026-5310
Preprint. Discussion started: 9 September 2026

		Naqu	4509	2021/6/1-2021/8/31	159	90
		SETS	3328	2021/6/1-2021/8/31	172	87
YKW3, Shanghai Leitan Technology Co., Ltd	Sichuan	Ganzi	3394	2023/5/1-2026/4/14	2088	1578
		Hongyuan	3493	2023/5/1-2026/4/14	2096	1510
YKW2, Beijing Airda Electronic Equipment Co., Ltd.		Yibin	342	2023/8/16-2026/4/14	1832	1226
Total					**18028**	**14020**

2.2 Mobile GMWR observations

The mobile GMWR observations were obtained during MFOCAP over the TRSR, 17-31 July 2021 (Cheng et al., 2024). The mobile observation system was equipped with an MWP967KV GMWR (Xi'an Electronic Engineering Research Institute, China), which continuously measured multichannel TBs at 22–58 GHz with a 30 s sampling interval. To ensure consistency with the fixed-site GMWR inputs, the same TB channels were selected as retrieval model inputs. The observation route passed through Xining, Dari, and Yushu in southeastern Qinghai, with most sections above 3500 m (Fig. 1).

2.3 Radiosonde observations

Radiosonde observations are taken twice daily (08:00 and 20:00 BT), providing vertical profiles of WS, wind direction, air temperature, relative humidity, and air pressure. For the 14 fixed-site GMWR, concurrent Raob from nearby stations were used, and WS at 13 pressure levels (350, 400, 450, 500, 525, 550, 575, 600, 625, 650, 675, 700, and 750 hPa) were extracted as output labels for the WP retrieval model.

Raob from Xining (2262 m a.s.l.), Dari (3968 m a.s.l.), and Yushu (3682 m a.s.l.) served as evaluation data for the mobile GMWR retrievals. The radiosonde WPs were collocated with the mobile observations in space and time, and data at the same 13 pressure levels were extracted, yielding 22 matched profiles. Given the limited number of Raob samples for evaluating the mobile GMWR retrievals, Raob-corrected ERA5 WPs were also used as independent evaluation data. A linear correction model, based on 186 Raob WPs (Xining, Dari, Yushu; 1–31 July 2021) matched with ERA5 data at nine pressure levels (350–750 hPa), was applied to correct the ERA5 WPs along the mobile route during MFOCAP.

https://doi.org/10.5194/egusphere-2026-5310
Preprint. Discussion started: 9 September 2026

2.4 ERA5 Reanalysis data

ERA5 reanalysis WP data from the European Centre for Medium-Range Weather Forecasts (ECMWF) were used for Xining, Dari, and Yushu during 1–31 July 2021, at 1-hour and 0.25° × 0.25° resolution. WPs at the same nine pressure levels as the Raob were extracted. Using the above-described ERA5 correction model, ERA5 data were matched to the mobile observations during MFOCAP by nearest grid point and time, and were subsequently corrected. A total of 204 WPs were available for evaluating the mobile GMWR retrieval accuracy.

3. Data Processing

3.1 TB QC

To ensure TB data reliability, QC was applied separately to fixed-site and mobile GMWR observations. For the 14 fixed-site GMWR, precipitation-affected data removal, outlier detection, and temporal consistency checks were applied sequentially to reduce the effects of precipitation and instrumental anomalies. Mobile GMWR observations may also be affected by obstruction from tunnels, bridges, and other structures, vehicle speed, and antenna pointing deviations due to platform vibration and tilt. Observation logs and synchronized inertial navigation system (INS) data were therefore used to identify obstruction and vehicle-speed effects, and to correct antenna pointing. The detailed QC procedures are described below:

(1) Removal of Precipitation-Affected Data

During precipitation, increased atmospheric water vapor absorbs microwave radiation, causing signal attenuation and reducing the accuracy of TB measurements. Therefore, precipitation-affected observations were removed following Thomas et al. (2025):

a. When 6-h accumulated precipitation ≥ 5 mm, observations within 30 min after the event were removed;

b. When 6-h accumulated precipitation > 0 and < 5 mm, observations within 15 min after the event were removed.

$$R(n) = \begin{cases} [T_e(n), T_e(n) + 30], & P(n) \geq 5 \\ [T_e(n), T_e(n) + 15], & 0 < P(n) < 5 \end{cases} \tag{1}$$

where $R(n)$ is the removal time range for the nth observation; $P(n)$ is the 6-h accumulated precipitation; and $T_e(n)$ is the end time of the corresponding precipitation event.

(2) Outlier removal

a. Outlier Detection

Outlier detection was based on the variability among four consecutive data points: a point was flagged if its difference from any of the next three points exceeded a threshold. Let TB_i be the TB at the ith point. Then:

$$|TB_i - TB_{i+a}| > const, a \in \{1,2,3\} \tag{2}$$

https://doi.org/10.5194/egusphere-2026-5310
Preprint. Discussion started: 9 September 2026

where TB_i and TB_{i+a} are the TBs at the i_{th} and $(i+a)_{\text{th}}$ data points, respectively. The thresholds, set to 8.0 K for K channels and 1.0 K for V channels, were determined by analyzing TB differences between adjacent data points during periods of good data quality and verified using typical anomalous samples.

b. Temporal Consistency Check

First, the k-sigma method was applied for preliminary QC of the observed TB. Let $TB(n)$ denote the TB time series, and $J(n)$ be a Boolean array indicating whether a data point was flagged as an outlier:

$$J(n) = \begin{cases} 1, |TB(n) - \mu| \geq k\sigma \\ 0, |TB(n) - \mu| < k\sigma \end{cases} \tag{3}$$

where μ and σ are the mean and standard deviation of $TB(n)$, respectively, and k is the threshold multiplier. Here, the 3-sigma method was used, with $J(n) = 1$ outliers and $J(n) = 0$ for retained data.

c. Obstacle Obstruction Check

After 3-sigma screening, short- and long-term TB fluctuations were examined based on 3- and 13-point moving windows, respectively.

$$\frac{std(x_{i-1}, x_i, x_{i+1})}{\sigma} \geq 1.6 \tag{4}$$

$$\frac{std(x_{i-6}, x_{i-5}, \cdots, x_{i+6})}{std(x_{i-1}, x_i, x_{i+1})} \leq const \tag{5}$$

where $std(x_{i-1}, x_i, x_{i+1})$ is the standard deviation of three consecutive data points, σ is the standard deviation of the entire dataset, and $std(x_{i-6}, x_{i-5}, \cdots, x_{i+6})$ is the standard deviation of 13 consecutive data points. A point was flagged as an outlier when the short-term SD substantially exceeded the long-term SD, with thresholds of 0.8 and 0.5 for low- and high-frequency channels, respectively, based on the statistical distribution under normal conditions.

(3) Vehicle Speed Impact Check

For mobile GMWR observations, vehicle speed is a key factor affecting TB accuracy. Because GMWR measurements require a finite integration time, vehicle speed directly influences the spatial representativeness and the degree of beam overlap between adjacent sampling points. Following Lei et al. (2023), a typical GMWR (~5° beamwidth, 10 km height) has a horizontal resolution of ~900 m, corresponding to ~108 km h^{-1} at a 30 s sampling interval. Synchronized INS vehicle-speed measurements during 17–31 July 2021 were therefore used to identify and remove abnormal TB observations.

(4) Antenna Pointing Correction

During mobile observations, platform vibration and tilt may alter the platform attitude and cause antenna pointing deviations, introducing biases into the received signals. Therefore, antenna pointing was corrected using synchronized INS attitude angles measurements to correct the TB observations following Corbella et al. (2001).

https://doi.org/10.5194/egusphere-2026-5310
Preprint. Discussion started: 9 September 2026

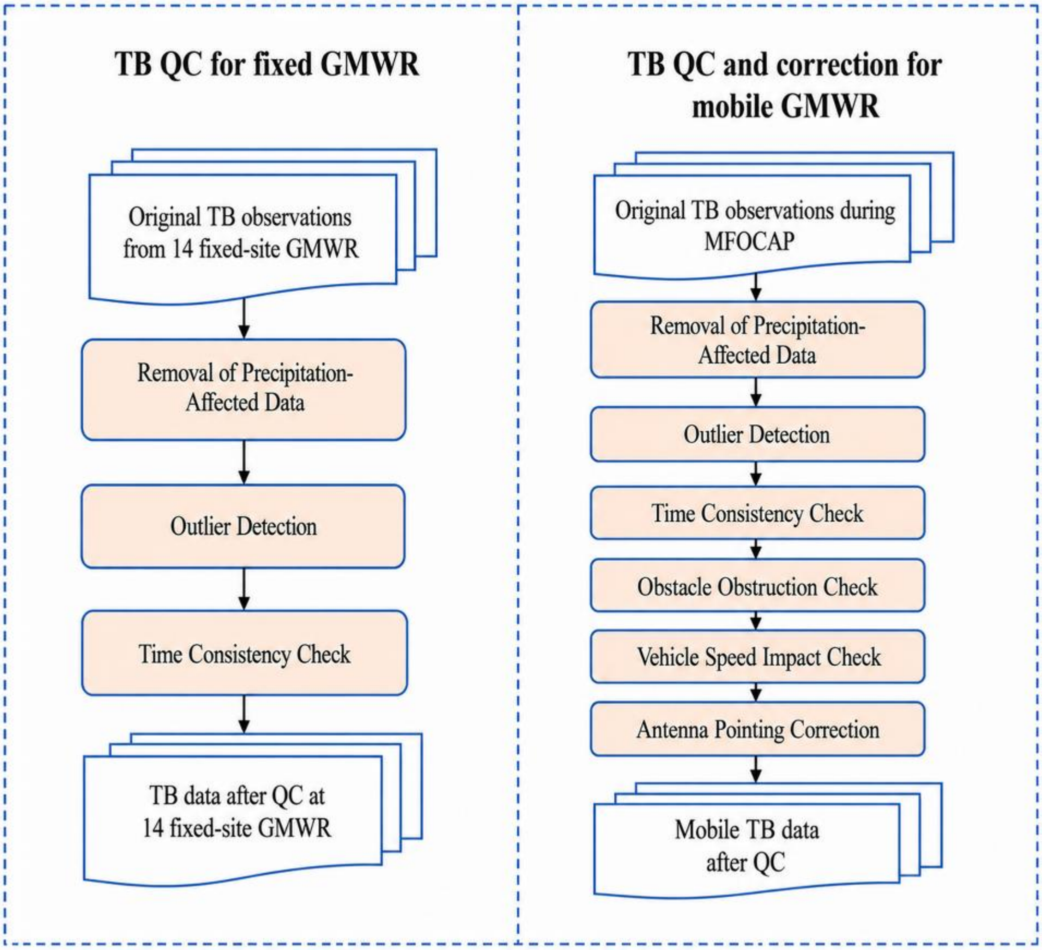

Figure 2: QC procedures for TB observations from fixed and mobile GMWR.

Given that mobile TB observations are subject to more interferences than fixed-site GMWR, their QC procedure is more complex; therefore, we focus only on the QC performance for the mobile TB data during the MFOCAP. Figure 3 compares the TB data before and after QC for different K/V-band channels during the MFOCAP. While the four K-band TB time series generally exhibit consistent temporal patterns, the raw observations suffer from considerable fluctuations and marked outliers. In general, the four V-band TB time series exhibit smaller fluctuations than the K-band channels, but abrupt anomalies before QC associated with platform vibration, signal interference, and obstacle obstruction are still evident. After QC, these anomalous values are effectively removed, resulting in more stable and continuous TB time series and providing more reliable inputs for the WP retrieval model.

https://doi.org/10.5194/egusphere-2026-5310
Preprint. Discussion started: 9 September 2026

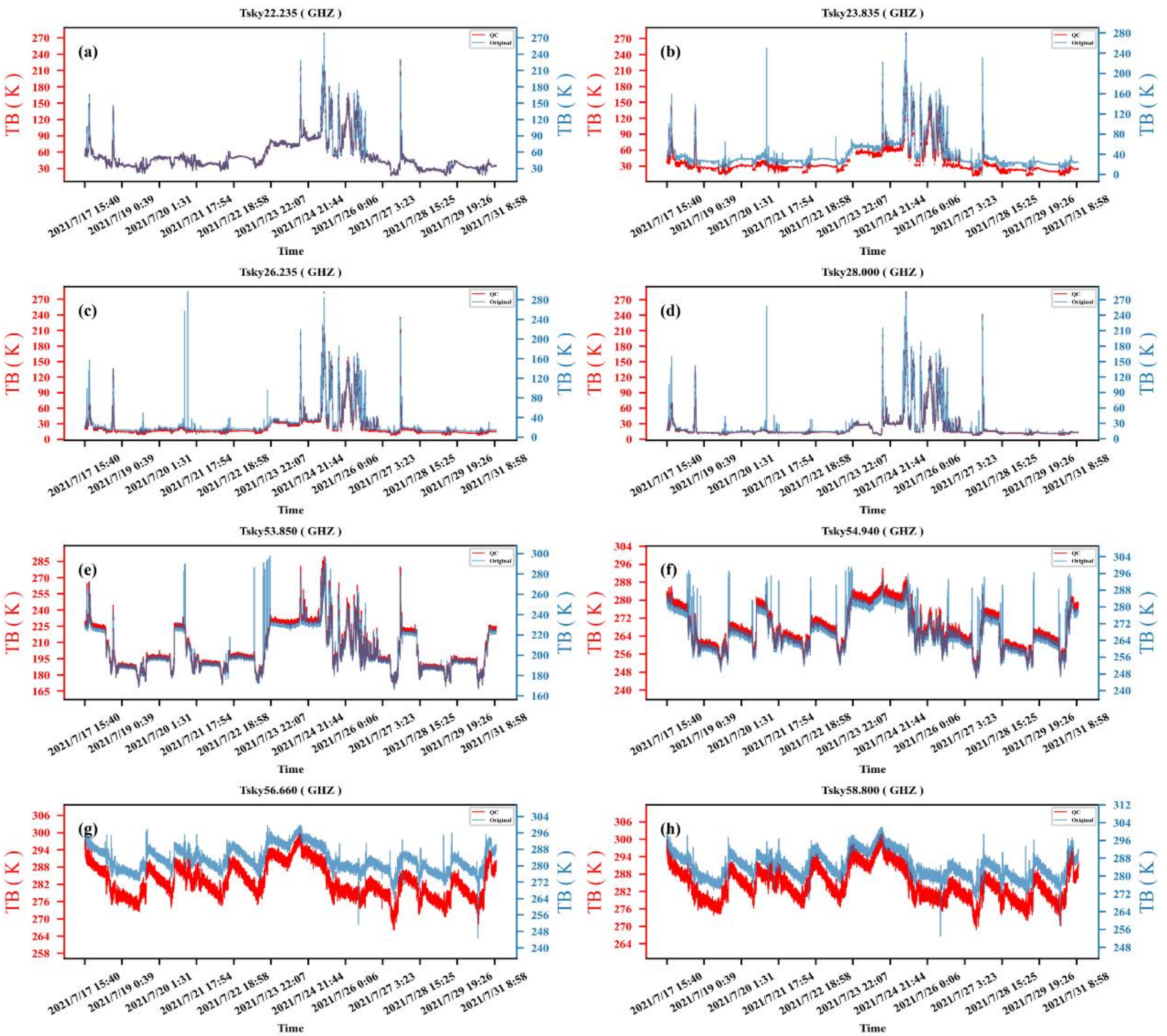

Figure 3: Time series of mobile GMWR TBs before and after QC for (a–d) K-band and (e–h) V-band channels over the Three-River Source Region during 17–31 July 2021. The blue and red lines represent the original and QC TB observations, respectively.

3.2 Distribution Alignment

Differences in instrument type, observation environment, and elevation caused TB feature distribution shifts between fixed-site and mobile GMWR observations. Three distribution-alignment methods (Quantile Transformer, PCA Whitening, and RankGauss) were evaluated to reduce their impact on generalization. The transformers were fitted on the 70% training set and then applied to the 10% validation set, 20% test set, and mobile GMWR dataset. Quantile Transformer reduced the

https://doi.org/10.5194/egusphere-2026-5310
Preprint. Discussion started: 9 September 2026

influence of extreme values in marginal distributions, PCA Whitening decorrelated the channels, and RankGauss mapped skewed variables to approximately Gaussian distributions while mitigating the effects of non-Gaussianity and outliers (Qi et al., 2024; Kessy et al., 2018; Deng, 2025). The optimal method was selected independently for each pressure level based on the retrieval errors.

(1) Quantile Transformer

Quantile Transformer is a nonparametric transformation technique based on quantile mapping. The empirical cumulative distribution function (ECDF) was first used to estimate the cumulative probability of each sample, followed by the inverse CDF of the standard normal distribution to map the original features to an approximately Gaussian distribution:

$$z = \Phi^{-1}\big(F(x)\big) \tag{6}$$

where x denotes the original TB feature, $F(x)$ its ECDF, $\Phi^{-1}(\cdot)$ the inverse cumulative distribution function of the standard normal distribution, and Z the transformed feature. This transformation mitigates distribution shifts between fixed and mobile observations.

(2) PCA Whitening

PCA Whitening decorrelates the input features via PCA and rescales each principal component by its eigenvalue to yield transformed components with unit variance. The covariance matrix is given by:

$$\Sigma = \frac{1}{N} X^T X \tag{7}$$

where X is the centered input-feature matrix and N is the number of samples.

The covariance matrix is then eigendecomposed as

$$\Sigma = U \Lambda U^T \tag{8}$$

where U is the eigenvector matrix and Λ is the diagonal matrix of eigenvalues. The whitened features are obtained as

$$X_w = X U \Lambda^{-\frac{1}{2}} \tag{9}$$

where X_w denotes the whitened data.

(3) RankGauss

RankGauss first ranks the samples by their values and then assigns the ranks to a standard normal distribution. Unlike direct standardization, this transformation preserves sample rank order while reducing outlier influence on training.

The sample quantile is first calculated as

$$r_i = \frac{rank(x_i) - 0.5}{N} \tag{10}$$

where N is the total number of samples and $rank(x_i)$ is the rank of the ith sample. The corresponding standard normal variable is then derived via the inverse error function:

$$z_i = \sqrt{2}\, erf^{-1}(2r_i - 1) \tag{11}$$

where erf^{-1} denotes the inverse error function.

https://doi.org/10.5194/egusphere-2026-5310
Preprint. Discussion started: 9 September 2026

3.3 Savitzky–Golay Smoothing

To reduce short-term noise in GMWR TB observations and fluctuations in wind-speed labels, the input features and training labels were smoothed using Savitzky–Golay (SG) filtering (Savitzky and Golay, 1964). SG filtering fits a low-order polynomial in a moving window to suppress high-frequency noise while retaining peaks, slopes, and overall temporal variations. The 12 TB channels were smoothed using a second-order, 5-point SG filter, while the wind-speed labels at each pressure level used a 7-point window of the same order. The same TB filtering configuration was applied to both fixed-site GMWR and mobile MWR observations.

4. Retrieval Method

The WP retrieval procedure is shown in Fig. 4. Samples from each station were independently split 7:1:2 into training, validation, and test sets, then merged across stations to ensure fixed station-wise proportions and enable cross-station generalization evaluation. SG filtering was applied to the input features and training labels. At each pressure level, the optimal distribution-alignment method (Quantile Transformer, PCA Whitening, or RankGauss) was selected to reduce shifts between fixed and mobile GMWR observations. A nonlinear weighted regression loss was adopted to mitigate central tendency from the long-tailed WS distribution and improve retrieval performance across WS ranges. Finally, an XGBoost–CatBoost ensemble model was built and tested on mobile GMWR observations to assess its generalization.

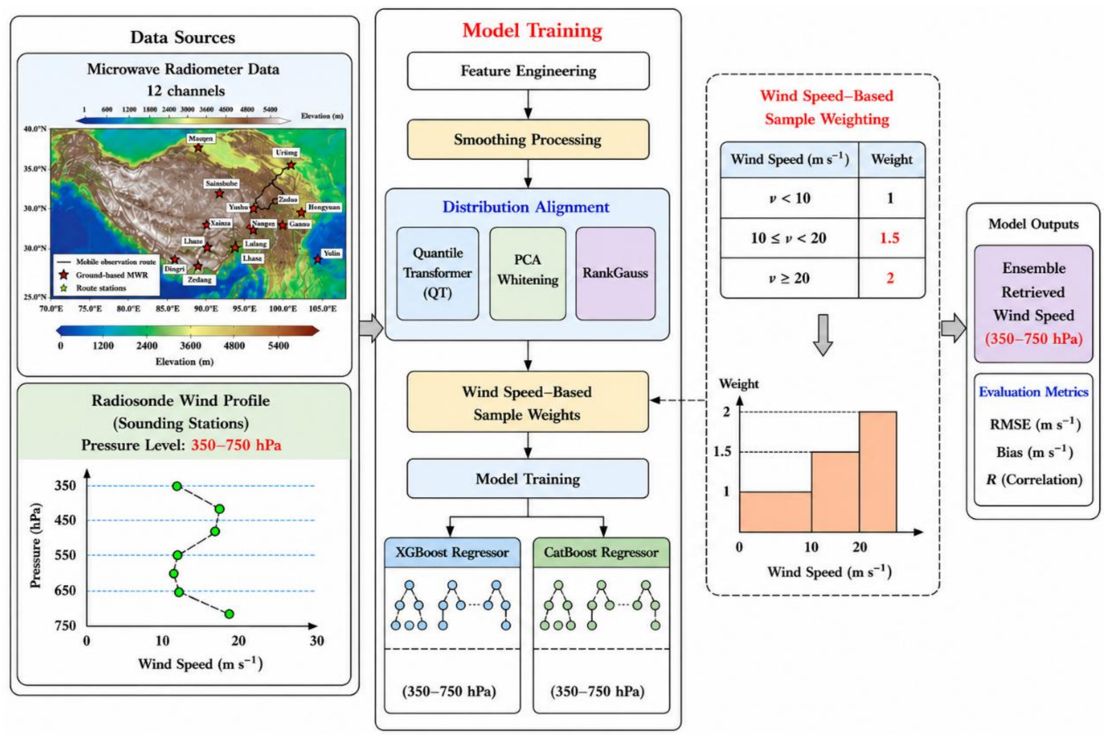

https://doi.org/10.5194/egusphere-2026-5310
Preprint. Discussion started: 9 September 2026

Figure 4: Flowchart of the WP retrieval algorithm.

4.1 Retrieval Model

XGBoost and CatBoost, two gradient-boosted tree models, were used to construct the WP retrieval model. XGBoost iteratively fits residuals in a gradient-boosting framework and employs regularization to penalize complexity and improve generalization (Chen and Guestrin, 2016). Its objective function is given by:

$$Obj = \sum_{i=1}^{N} l\,(y_i, \hat{y}_i) + \sum_{k=1}^{K} \Omega\,(f_k) \tag{12}$$

where $\Omega(f_k)$ is given by:

$$\Omega(f_k) = \gamma T + \frac{1}{2}\lambda \sum_{j=1}^{T} w_j^2 \tag{13}$$

here $l(\cdot)$ is the loss function, f_k is the kth decision tree, T is the number of leaf nodes, w_j is the weight of the jth leaf node, and γ and λ are regularization parameters.

CatBoost employs Ordered Boosting to reduce shift and symmetric trees to improve efficiency and generalization, offering stable performance for complex nonlinear relationships and small-to-medium datasets (Prokhorenkova et al., 2018). To utilize the complementary strengths of XGBoost and CatBoost, different ensemble weights were evaluated. The simple averaging ensemble outperformed the weighted alternatives in retrieval accuracy and stability on the validation set; thus, equal weighting was adopted.

4.2 Nonlinear Weighted Regression Loss

Due to the far greater number of low-wind than strong-wind samples in the Raob data, the model exhibits a central tendency, leading to underestimation of strong winds. To mitigate this, a three-level weighting scheme was defined based on WS:
For WS v, the sample weight $w(v)$ is defined as

$$w(v) = \begin{cases} 1, & v < 10\ m\ s^{-1} \\ 1.5, & 10 \le v < 20\ m\ s^{-1} \\ 2, & v \ge 20\ m\ s^{-1} \end{cases} \tag{14}$$

The weighted loss function used for model training is

$$L = \sum_{i=1}^{N} w_i\ l(y_i, \hat{y}_i) \tag{15}$$

where w_i is the sample weight, $l(\cdot)$ is the loss for an individual sample, y_i is the observed value, and $\hat{y}_i$ is the retrieved value.

https://doi.org/10.5194/egusphere-2026-5310
Preprint. Discussion started: 9 September 2026

5. Results

5.1 Fixed GMWR

5.1.1 Model Evaluation

To evaluate the reliability of the WP retrieval model, samples from each of the 14 fixed-site GMWR were independently divided into training, validation, and test datasets at a ratio of 7:1:2, and the corresponding subsets were then merged across stations to ensure representation of all stations in each subset. The correlation coefficient (R), root-mean-square error (RMSE), and mean absolute error (MAE) were used to evaluate retrieval accuracy. It is noteworthy that, due to the high elevation of some GMWR stations over the TP, fewer data are available for the 750–600 hPa pressure levels, which leads to a total sample number for the 13 pressure levels that is less than anticipated. Figure 5 compares the retrieved WS and Raob for the test dataset during the period from January 2021 to April 2026. The mean retrieved WS at each pressure level agreed well with the Raob but were slightly lower overall, possibly due to uncertainties in TB measurements, limited training samples, and radiosonde drift. RMSE increased with altitude, yet remained below 4.5 m s^{-1} overall and below 2.0 m s^{-1} in the lower troposphere (750–500 hPa). Fig. 5c shows that most data points lie near the 1:1 line, indicating good reproduction of WP spatiotemporal variability by the retrieval model. The scatter is denser for low winds but more spread for strong winds, without any notable systematic bias. Retrieved WS achieved strong performance (R=0.96, RMSE=2.24 m s^{-1}, MAE=1.57 m s^{-1}). These results demonstrate high retrieval accuracy and robustness across the multi-station test set, and provide a solid foundation for subsequent WP retrieval from mobile GMWR observations.

https://doi.org/10.5194/egusphere-2026-5310
Preprint. Discussion started: 9 September 2026

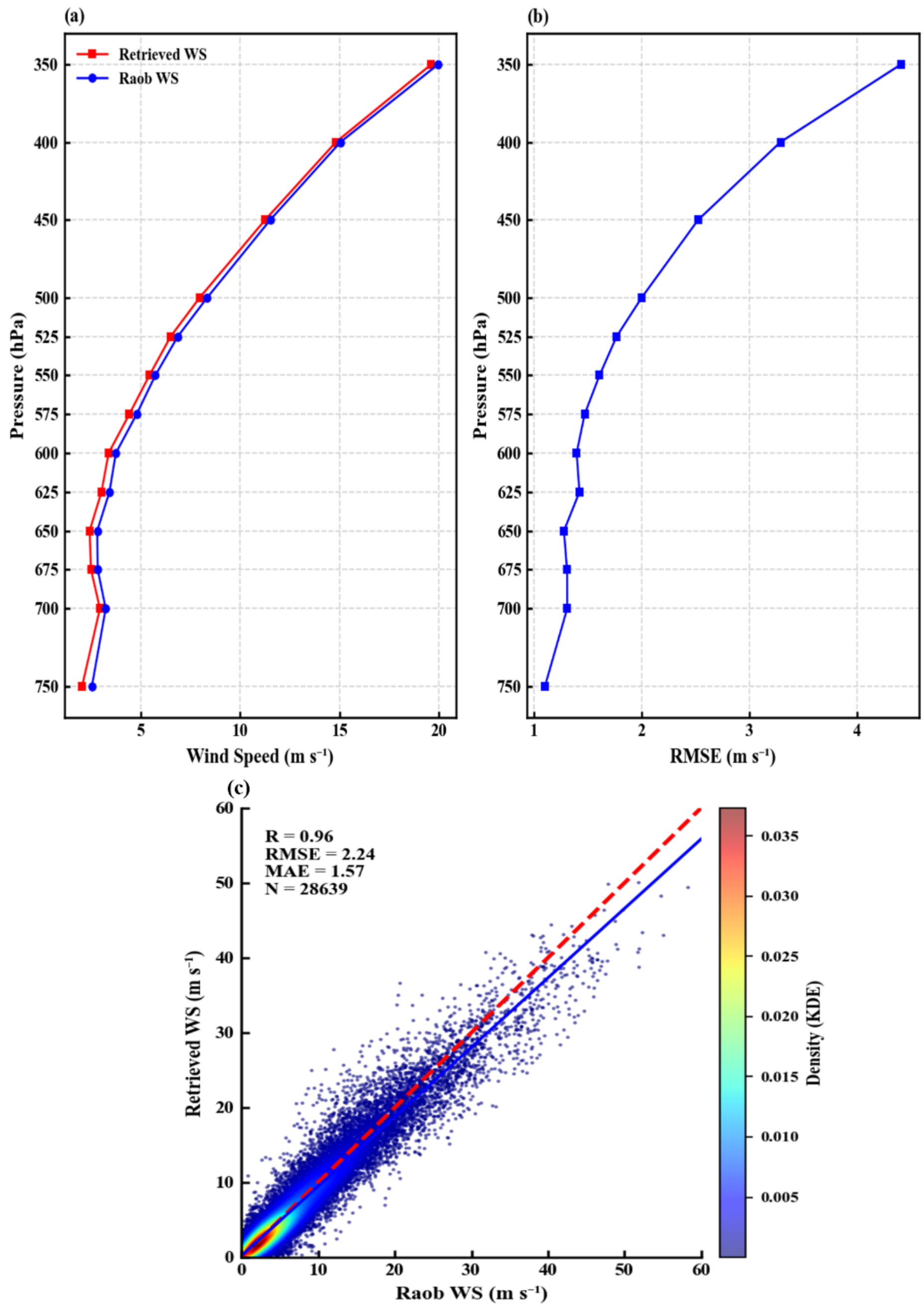

Figure 5: Vertical profiles of mean retrieved WS and Raob at each pressure level (a), the corresponding RMSE (b), and scatterplots (c) of retrievals vs. observations from the test set for 14 fixed-site GMWR over the TP, covering January 2021 to April 2026.

https://doi.org/10.5194/egusphere-2026-5310
Preprint. Discussion started: 9 September 2026

5.1.2 Impact Factors

Although Chen et al. (2024) examined the effects of weather conditions, diurnal variation of TB, and elevation on WP retrieval accuracy, their analysis was based on limited mobile data from 17-31 July 2021 and did not exclude rain-contaminated observations. Using a much larger and longer-term dataset—the 20% test set from 14 fixed-site GMWR over the TP from January 2021 to April 2026—this study re-examines these factors to better quantify their effects on retrieval errors and draw more robust conclusions.

(1) Weather conditions

Figure 6 compares retrieved and Raob WS under clear-sky and cloudy conditions for the test set from the 14 fixed-site GMWR over the TP from January 2021 to April 2026. According to the meteorological condition classification method (Cheng et al., 2014), samples were classified as clear-sky (total cloud cover, TCC < 20%) or cloudy (TCC≥ 20%). Under clear-sky conditions, R, RMSE, and MAE were 0.96, 1.99 m s^{-1}, and 1.49 m s^{-1}, respectively, compared with 0.95, 2.31 m s^{-1}, and 1.63 m s^{-1} under cloudy conditions. The WP retrieval model performs robustly under both clear-sky and cloudy conditions, with smaller retrieval errors during clear skies. The slightly larger retrieval errors under cloudy conditions may be associated with cloud liquid water, which contributes to microwave absorption and emission and thereby modifies the observed TBs (Turner et al., 2007).

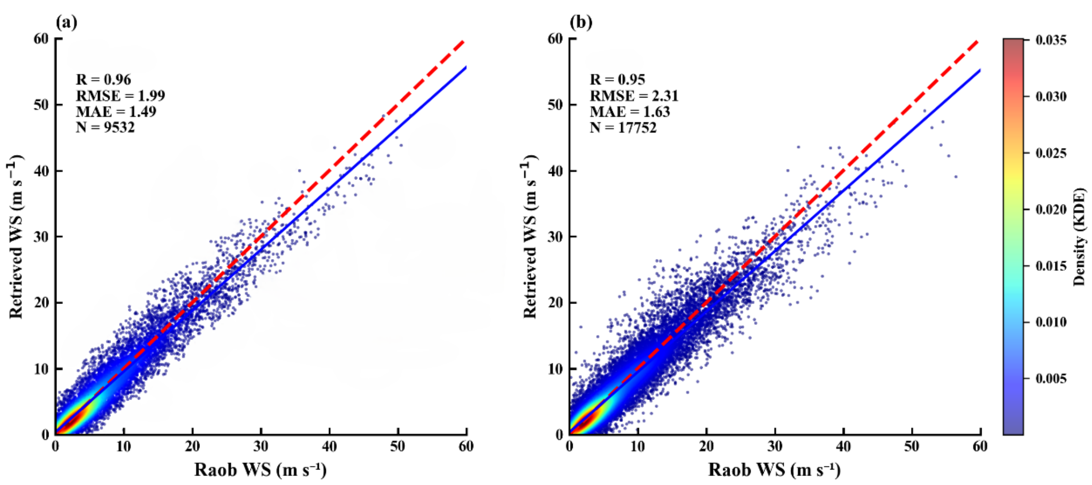

Figure 6: Scatterplots of retrieved WS against Raob observations under (a) clear-sky and (b) cloudy conditions for the test set of the 14 fixed-site GMWR over the TP from January 2021 to April 2026. The red and blue dashed lines denote the 1:1 reference and fitted regression lines, respectively.

To explore the effect of cloud cover on retrieval errors, the test samples were binned into five TCC ranges: 0.0–0.2, 0.2–0.4, 0.4–0.6, 0.6–0.8, and 0.8–1.0. The R, RMSE, and MAE between the retrieved and Raob WS were then calculated for each range. As shown in Table 2, R exceeded 0.94 across all TCC ranges, while retrieval errors generally increased with TCC. The lowest RMSE and MAE occurred in the 0.0–0.2 range, whereas the largest errors were found in the 0.8–1.0 range.

https://doi.org/10.5194/egusphere-2026-5310
Preprint. Discussion started: 9 September 2026

These results indicate that retrieval errors increase moderately with TCC, while the model maintains good correlation and stability across different cloud conditions.

Table 2: WS retrieval errors for different TCC ranges at the 14 fixed-site GMWR over the TP from January 2021 to April 2026.

TCC	R	RMSE (m s^{-1})	MAE (m s^{-1})
0.0-0.2	0.96	1.99	1.49
0.2-0.4	0.95	2.18	1.58
0.4-0.6	0.94	2.12	1.46
0.6-0.8	0.94	2.22	1.51
0.8-1.0	0.94	2.36	1.66

(2) Diurnal Variation of PBLH

To investigate the influence of diurnal variations of planetary boundary layer height (PBLH) on WP retrieval, the 20% test set from the 14 fixed-site GMWR over the TP (January 2021–April 2026) was divided into two groups according to Raob launch times: 08:00 and 20:00 BT. Figure 7 compares the vertical distributions of retrieved WS and Raob, and the corresponding RMSE at the two times. The retrieved WS agreed well with Raob across all pressure levels, with RMSE below 2.5 m s^{-1} for the 750–450 hPa layer at both observation times, indicating high retrieval accuracy in the mid-to-lower troposphere. Further comparison showed that RMSE of retrieved WS at 08:00 BT was generally lower than that at 20:00 BT within the 600–700 hPa layer, in agreement with Chen et al. (2024). In line with Cheng et al. (2024) regarding the imapct of the diurnal variation of PBLH on air temperature profile retrieval errors over the TP, nighttime radiative cooling reduces PBLH and stabilizes the atmosphere at 08:00 BT, allowing GMWR to obtain more consistent thermodynamic data and thus lowering errors. Conversely, daytime surface heating and PBL evolution at 20:00 BT produce a more variable thermodynamic structure, resulting in larger retrieval errors.

https://doi.org/10.5194/egusphere-2026-5310
Preprint. Discussion started: 9 September 2026

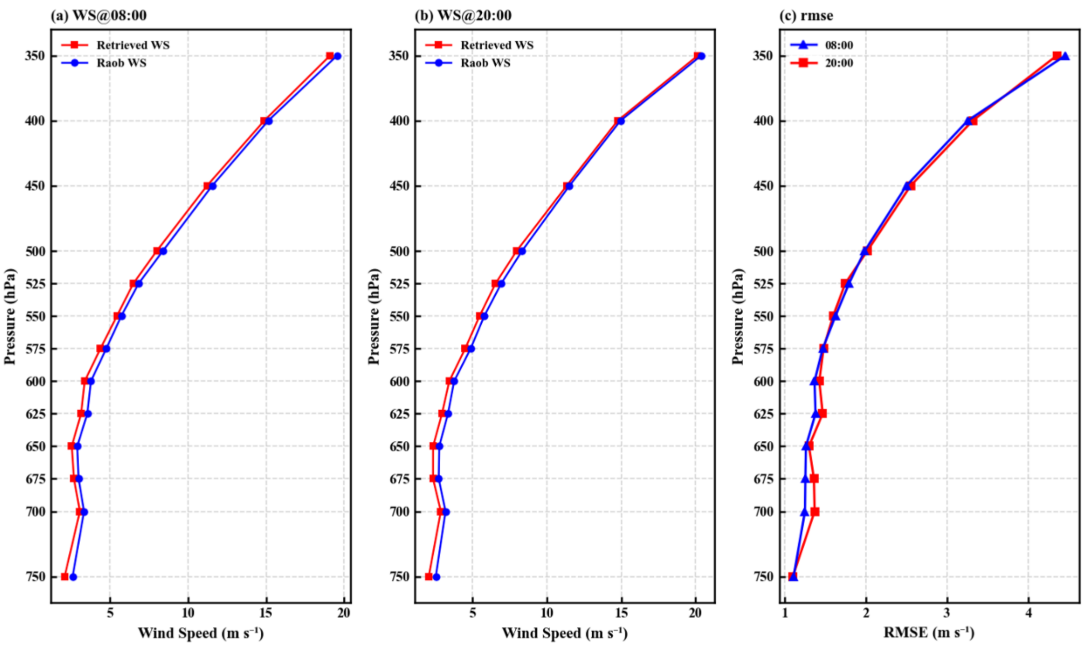

Figure 7: Vertical profiles of retrieved WS and Raob at 08:00 BT (a) and 20:00 BT (b), and the corresponding RMSE (c) for the test set from the 14 fixed-site GMWR over the TP (January 2021–April 2026).

(3) Elevation

To investigate the influence of elevation on retrieval accuracy, the 20% test set was divided into four groups according to station altitude. Table 3 presents the WS retrieval errors for different elevation ranges at the 14 fixed-site GMWR over the TP and its surrounding areas from January 2021 to April 2026. The retrieved WS generally agreed well with the Raob across all elevation ranges, with R exceeding 0.96. However, RMSE increased notably with elevation, with a particularly sharp rise at stations above 4 km, where RMSE exceeded 3.0 m s^{-1}. This finding is consistent with the results of Chen et al. (2024). This is likely due to lower water vapor and oxygen densities at high elevations, which attenuate microwave emission and amplify TB uncertainties, consequently increasing WP retrieval errors.

Table 3: WS retrieval errors for different elevation ranges at the 14 fixed-site GMWR over the TP from January 2021 to April 2026.

Elevation	R	RMSE (m s^{-1})	MAE (m s^{-1})
0-2 km	0.98	2.39	1.63
2-3 km	0.96	2.79	1.69
3-4 km	0.97	2.80	1.64
>4 km	0.97	3.03	1.95

https://doi.org/10.5194/egusphere-2026-5310
Preprint. Discussion started: 9 September 2026

5.2 Mobile GMWR Observations

To assess the model's generalization capability under mobile observations over the TRSR, we validated the retrieved WP against two independent references: (1) sparse but accurate Raob data from Xining, Dari, and Yushu, and (2) high-resolution Raob-corrected ERA5 reanalysis, over the period 17–31 July 2021. After spatiotemporal collocation, 22 radiosonde–GMWR matchups were identified. Owing to missing values at some pressure levels, the sample size for error statistics was further reduced; therefore, given the sensitivity of RMSE to extreme values in small samples, we adopted mean bias (MB) to evaluate the systematic bias of the retrievals against Raob and its vertical distribution. Given that ERA5 reanalysis is biased over the TP's complex terrain and unsuitable for direct evaluation of mobile GMWR retrievals, we instead applied Raob-corrected hourly ERA5 WP data for further validation.

5.2.1 Evaluation against Raob

Figure 8 shows the vertical distributions of mean retrieved WS and Raob at each pressure level, and the corresponding MB at three radiosonde stations during 17–31 July 2021. Overall, the retrieval model captured the vertical structure of WS well, showing strong agreement with Raob within the 700–450 hPa layer. Although retrieved WS was slightly overestimated over 700–400 hPa and underestimated at 350 hPa, the absolute MB at all levels remained below 2 m s^{-1}. These errors likely arise from TB measurement uncertainties, distribution-alignment procedures, limited training samples, and radiosonde drift, with future work aiming to refine and evaluate the model using more mobile observations.

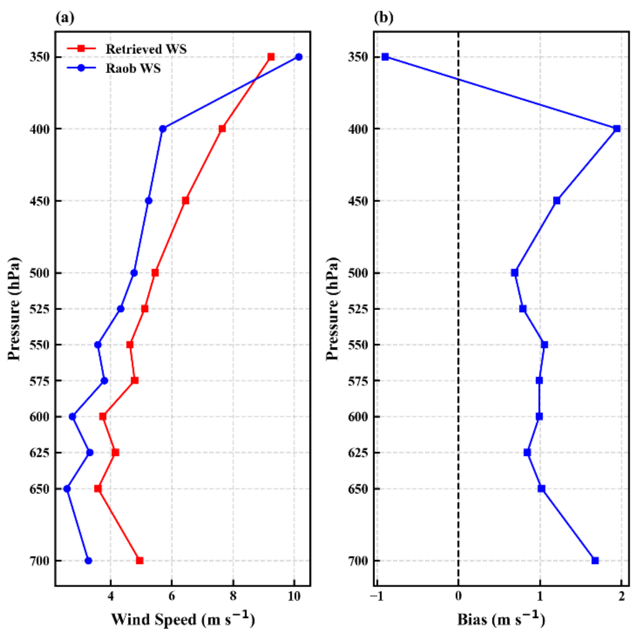

Figure 8: Vertical profiles of retrieved WS and Raob (a), and corresponding MB (b) at Xining, Dari and Yushu radiosonde stations during 17–31 July 2021.

https://doi.org/10.5194/egusphere-2026-5310
Preprint. Discussion started: 9 September 2026

5.2.2 Evaluation based on Raob-corrected ERA5

The Raob-corrected ERA5 WS, offering more complete spatiotemporal coverage than sparse Raob, serve as a complementary reference for evaluating retrieval performance during continuous mobile observations. Figure 9 shows vertical distributions of retrieved WS and Raob-corrected ERA5, and the corresponding RMSE along the mobile observation route over the TRSR during MFOCAP. Although retrieved WS were generally higher than corrected ERA5 winds at all levels, RMSE remained below 4.0 m s^{-1} , with values exceeding 3.0 m s^{-1} only in the 700–750 hPa and 350–450 hPa layers and smaller elsewhere. The larger errors may partly result from limited training samples, which restrict the model's ability to capture wind-field variability at these levels, along with uncertainties in the corrected ERA5 wind profiles.
Figure 9c presents the scatterplot of retrieved WS against corrected ERA5 data along the mobile observation route during MFOCAP. The two datasets show an overall correlation of 0.66, with RMSE and MAE of 2.66 and 2.25 m s^{-1}, respectively, and most samples fall within the low-to-moderate WS range (≤7.5 m s^{-1}). Retrieved WS exhibited a systematic bias—overestimated at low WS and increasingly underestimated as WS increased. This bias likely stems from TB distribution differences between the fixed-site training data and mobile observations. Despite smoothing and distribution alignment, some domain shift remained, so that mobile samples deviating from the training distribution caused retrievals to regress toward the densely sampled wind-speed range—overestimating weak winds and underestimating strong ones.

https://doi.org/10.5194/egusphere-2026-5310
Preprint. Discussion started: 9 September 2026

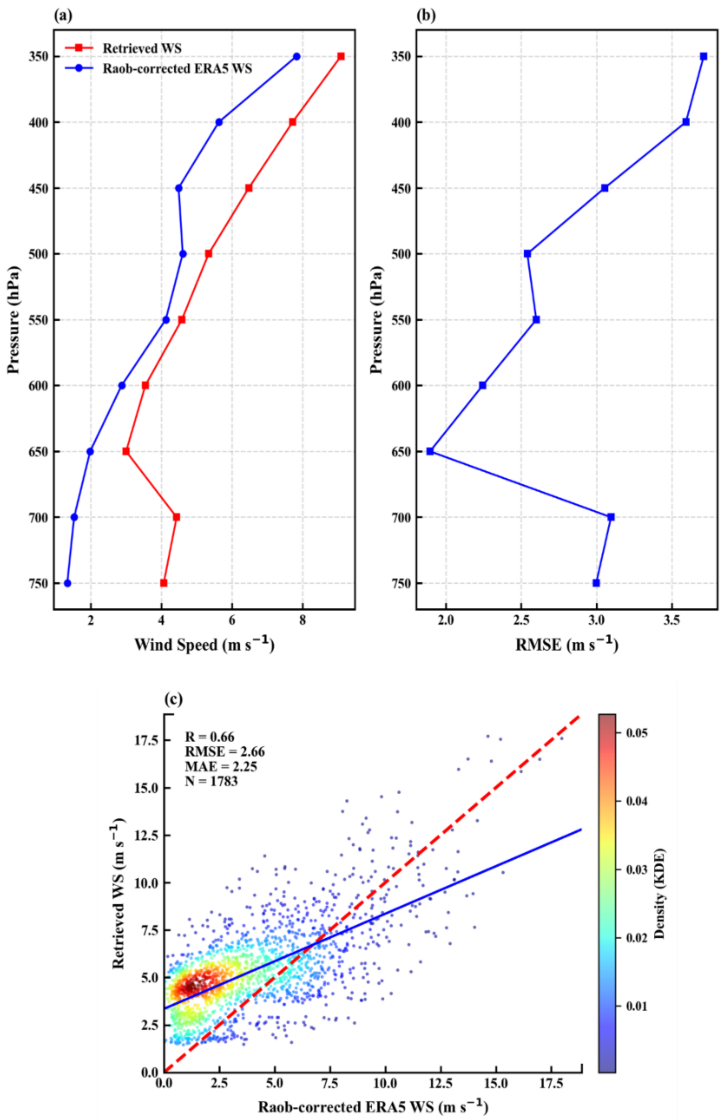

Figure 9: Vertical profiles of (a) retrieved WS and Raob-corrected ERA5, (b) corresponding RMSE, and (c) scatterplot of retrieved WS against corrected ERA5, along the mobile observation route over the TRSR during 17–31 July 2021. The dashed line in (c) denotes the 1:1 reference.

6. Conclusions and Discussion

To address the limited temporal frequency and spatial continuity of WP observations over the TP, this study developed a ground-based WP retrieval model using GMWR TB data. The model employs an equally weighted ensemble of XGBoost and CatBoost, trained on TB data from 14 fixed GMWR sites and radiosonde-derived WP, and then applied to retrieve mobile WP during the MFOCAP. The retrieval framework incorporated strict QC of TB data, station-wise dataset

https://doi.org/10.5194/egusphere-2026-5310
Preprint. Discussion started: 9 September 2026

partitioning, data smoothing, pressure-level-specific distribution alignment, and a wind-speed-weighted regression loss function. In addition, the impacts of weather conditions, diurnal variations of PBLH and station elevation on retrieval performance were systematically examined. These methodological designs collectively improve retrieval accuracy while enhancing model robustness and generalization capability across diverse observational settings and geographic regions within the plateau.

The model demonstrated robust retrieval performance across both fixed-site and mobile observations. For the 14 fixed-site GMWR, retrieved WS showed a correlation of 0.96 with Raob, with RMSE and MAE of 2.24 and 1.57 m s^{-1}, respectively; RMSE remained below 2.0 m s^{-1} in the lower troposphere (750–500 hPa). Mobile GMWR retrievals over the TRSR reproduced the vertical WS structure well, with mean absolute bias against Raob generally below 2 m s^{-}. Against Raob-corrected ERA5 WP, the retrievals achieved a correlation of 0.66, with RMSE and MAE of 2.66 and 2.25 m s^{-1}, respectively, and RMSE below 4.0 m s^{-1} at all pressure levels. However, the retrievals still exhibited a systematic bias, overestimating weak winds and underestimating strong ones.

Overall, the ensemble framework effectively retrieves continuous WP over large regions based on mobile observations with GMWR. Uncertainties at high altitudes and for strong winds likely stem from TB measurement errors, distribution-alignment issues, limited samples, and radiosonde drift. To further improve model accuracy, stability, and generalization capability over the TP's complex terrain, future efforts will collect more observations in under-represented regimes and develop dedicated retrieval models tailored to different WS and elevation ranges.

Data availability

The measured MO data of TB after quality control presented in this paper are available from Cheng (2024). The ERA5 reanalysis data are publicly available at https://cds.climate.copernicus.eu/cdsapp#!/dataset/reanalysis-era5-pressure-levels?tab=form. The surface and upper-level meteorological data including rainfall amount and WS data are available at https://data.cma.cn.

Author contributions

Y. Ma conducted the experiments, performed the data analysis, and led the manuscript writing. X. Cheng contributed to the experimental design and provided the Mobile GMWR observation dataset. J. Mao acquired the GMWR dataset for the study. G. Xu supervised the research. N. Li performed data quality control. B. Chen contributed supplementary technical methodologies. All authors reviewed and edited the final manuscript.

https://doi.org/10.5194/egusphere-2026-5310
Preprint. Discussion started: 9 September 2026

Competing interests

The contact author has declared that none of the authors has any competing interests

Acknowledgements

This work was supported by Tibet Autonomous Region Science and Technology Department (grant no. XZ202601ZY0196), the R&D major projects from China State Railway Group Co., Ltd. (grant no. K2022G039), and the Science and Technology Development Fund of the Chinese Academy of Meteorological Sciences (grant no. 2026GJ38). The authors acknowledge Professor Xuelong Chen from the Institute of Tibetan Plateau Research, Chinese Academy of Sciences, for providing the fixed ground-based microwave radiometer observation data.

References

Chen, B., Cheng, X. H., Su, D. B., Xu, X. D., Ma, S. Y., and Hu, Z. Q.: Wind profile retrieval based on LSTM algorithm and mobile observation of brightness temperature over the Tibetan Plateau, Remote Sens., 16, 1068, https://doi.org/10.3390/rs16061068, 2024.

Chen, H. B., Lu, D. R., Wei, C., and Liu, J.: Comparison of the effects of different microwave channel combinations and TB functions in the algorithm for retrieving precipitable water in the clear atmosphere, Chinese J. Atmos. Sci., 20, 757–762 (in Chinese), 1996.

Chen, T. and Guestrin, C.: XGBoost: A scalable tree boosting system, Proc. 22nd ACM SIGKDD Int. Conf. on Knowledge Discovery and Data Mining, ACM, 785–794, https://doi.org/10.1145/2939672.2939785, 2016.

Chen, X., Liu, Y., Ma, Y., Ma, W., Xu, X., Cheng, X., Li, L., Xu, X., and Wang, B.: TP-PROFILE: Monitoring the thermodynamic structure of the troposphere over the Third Pole, Adv. Atmos. Sci., 41, 1264–1277, https://doi.org/10.1007/s00376-023-3199-y, 2024.

Cheng, X., Xu, X., Bai, G., Wang, R., Ma, J., Su, D., Chen, B., Ma, S., Hu, C., Zhang, S., Zhao, R., Yang, H., Cheng, S., Zhang, W., Wang, S., and Xie, G.: Mobile observation field experiment of atmospheric vertical structure and its application in precipitation forecasts over the Tibetan Plateau, J. Geophys. Res. Atmos., 129, e2024JD042467, https://doi.org/10.1029/2024JD042467, 2024.

Cheng, X., Su, D., Li, D., Chen, L., Xu, W., Yang, M., Li, Y., Yue, Z., and Wang, Z.: An improved method for correction of air temperature measured using different radiation shields, Adv. Atmos. Sci., 31, 1460–1468, https://doi.org/10.1007/s00376-014-3129-0, 2014.

https://doi.org/10.5194/egusphere-2026-5310
Preprint. Discussion started: 9 September 2026

Corbella, I., Gasiewski, A. J., Klein, M., and Piepmeier, J. R.: Compensation of elevation angle variations in polarimetric brightness temperature measurements from airborne microwave radiometers, IEEE Trans. Geosci. Remote Sens., 39, 193–195, https://doi.org/10.1109/36.898683, 2001.

Deng, M., Zhang, C., Tang, M., Liao, C., Hu, Y., Zhang, Z., Feng, S., and Zheng, Z.: Stacking ensemble learning coupled with multi-source remote sensing data: Enhancing soil salinity inversion accuracy in barley-cultivated salinized soils, Agricultural Water Management, 322, 109959, https://doi.org/10.1016/j.agwat.2025.109959, 2025.

Deng, X.: Enhancing neural network performance on tabular data via knowledge distillation and RankGauss transformation, Proc. 6th Int. Conf. on Big Data & Artificial Intelligence & Software Engineering (ICBASE), IEEE, 418–423, https://doi.org/10.1109/ICBASE66587.2025.11181427, 2025.

Hogg, D. C., Decker, M. T., Guiraud, F. O., Earnshaw, K. B., Merritt, D. A., Moran, K. P., Sweezy, W. B., Strauch, R. G., Westwater, E. R., and Little, C. G.: An automatic profiler of the temperature, wind and humidity in the troposphere, J. Climate Appl. Meteor., 22, 807–831, https://doi.org/10.1175/1520-0450(1983)022<0807:AAPOTT>2.0.CO;2, 1983.

Huang, Y. B., Ligeer, D., and Wang, Z. H.: Remote sensing of atmospheric cloud water over the Tibetan Plateau using a ground-based dual-channel microwave radiometer, J. Nanjing Inst. Meteor., 24, 391–397 (in Chinese), 2001.

Jiang, S., Ma, Y., Li, C., Lei, L., Liu, B., Jin, S., Li, H., Wang, W., Fan, R., Wang, Y., Miao, A., and Gong, W.: Passive atmospheric wind profile retrieval via multi-region microwave radiometer network, Atmos. Res., 329, 108474, https://doi.org/10.1016/j.atmosres.2025.108474, 2026.

Karan, H. and Knupp, K. R.: Mobile Integrated Profiler System (MIPS) observations of low-level convergent boundaries during IHOP, Mon. Wea. Rev., 134, 92–112, https://doi.org/10.1175/MWR3058.1, 2006.

Kessy, A., Lewin, A., and Strimmer, K.: Optimal whitening and decorrelation, Amer. Stat., 72, 309–314, https://doi.org/10.1080/00031305.2016.1277159, 2018.

Kuang, X. and Jiao, J. J.: Review on climate change on the Tibetan Plateau during the last half century, J. Geophys. Res. Atmos., 121, 3979–4007, https://doi.org/10.1002/2015JD024728, 2016.

Lei, L. F., Li, C. W., Bai, S. C., Jiang, H. L., Wang, Z. H., and Lu, J. P.: Mobile atmospheric transect observations with a vehicle-mounted microwave radiometer and preliminary applications, Desert Oasis Meteor., 17, 1–9 (in Chinese), https://doi.org/10.12057/j.issn.1002-0799.2023.05.001, 2023.

Li, L., Zhang, P. L., Shen, H. Y., Li, J. G., and Jian, Y.: Spatiotemporal variation and mechanisms of water-vapor transport over the Three-River Source Region, Plateau Mountain Meteor. Res., 41, 9–16 (in Chinese), https://doi.org/10.3969/j.issn.1674-2184.2021.01.002, 2021.

Liu, B., Guo, J., Gong, W., Shi, L., Zhang, Y., and Ma, Y.: Characteristics and performance of wind profiles as observed by the radar wind profiler network of China, Atmos. Meas. Tech., 13, 4589–4600, https://doi.org/10.5194/amt-13-4589-2020, 2020.

https://doi.org/10.5194/egusphere-2026-5310
Preprint. Discussion started: 9 September 2026

Liu, L., Zheng, J., Ruan, Z., Cui, Z., Hu, Z., Wu, S., Dai, G., and Wu, Y.: Integrated radar observations of clouds and precipitation over the Tibetan Plateau in 2014 and preliminary cloud characteristics, Acta Meteor. Sinica, 73, 635–647 (in Chinese), https://doi.org/10.1007/s13351-015-4208-6, 2015.

Liu, N., Shen, Y., Zhang, S., and Zhu, X.: Establishment and evaluation of atmospheric water vapor inversion model without meteorological parameters based on machine learning, Sensors, 25, 420, https://doi.org/10.3390/s25020420, 2025.

Ma, Z., Li, J., Han, W., Li, Z., Zeng, Q., Menzel, W. P., Schmit, T. J., Di, D., and Liu, C.: Four-dimensional wind fields from geostationary hyperspectral infrared sounder radiance measurements with high temporal resolution, Geophys. Res. Lett., 48, e2021GL093794, https://doi.org/10.1029/2021GL093794, 2021.

Minola, L., Zhang, G., Ou, T., Kukulies, J., Curio, J., Guijarro, J. A., Deng, K., Azorin-Molina, C., Shen, C., Pezzoli, A., and Chen, D.: Climatology of near-surface wind speed from observational, reanalysis and high-resolution regional climate model data over the Tibetan Plateau, Climate Dyn., 62, 933–953, https://doi.org/10.1007/s00382-023-06931-3, 2024.

Ou, T., Chen, D., Tang, J., Lin, C., Wang, X., Kukulies, J., and Lai, H. W.: Wet bias of summer precipitation in the northwestern Tibetan Plateau in ERA5 is linked to overestimated lower-level southerly wind over the plateau, Climate Dyn., 61, 2139–2153, https://doi.org/10.1007/s00382-023-06672-3, 2023.

Prokhorenkova, L., Gusev, G., Vorobev, A., Dorogush, A. V., and Gulin, A.: CatBoost: Unbiased boosting with categorical features, Adv. Neural Inf. Process. Syst., 31, 2018.

Qi, D., Peng, J., He, Y., and Wang, J.: Auto-FP: An experimental study of automated feature preprocessing for tabular data, Proc. 27th Int. Conf. on Extending Database Technology (EDBT), 129–142, 2024.

Savitzky, A. and Golay, M. J. E.: Smoothing and differentiation of data by simplified least squares procedures, Anal. Chem., 36, 1627–1639, https://doi.org/10.1021/ac60214a047, 1964.

Stogryn, A. P., Butler, C. T., and Bartolac, T. J.: Ocean surface wind retrievals from Special Sensor Microwave Imager data with neural networks, J. Geophys. Res. Oceans, 99, 981–984, https://doi.org/10.1029/93JC03042, 1994.

Su, Z., Wen, J., Zeng, Y., Zhao, H., Lv, S., van der Velde, R., Zheng, D., Wang, X., Wang, Z., Schwank, M., Kerr, Y., Yueh, S., Colliander, A., Qian, H., Drusch, M., and Mecklenburg, S.: Multiyear in-situ L-band microwave radiometry of land surface processes on the Tibetan Plateau, Scientific Data, 7, 317, https://doi.org/10.1038/s41597-020-00657-1, 2020.

Thomas, G., Martinet, P., Brousseau, P., Chambon, P., Georgis, J., Hervo, M., Huet, T., Löhnert, U., Orlandi, E., and Unger, V.: Assimilation of ground-based microwave radiometer temperature observations into a convective-scale NWP model for fog forecast improvement, Quart. J. Roy. Meteor. Soc., 151, e4893, https://doi.org/10.1002/qj.4893, 2025.

Turner, D. D., Clough, S. A., Liljegren, J. C., Clothiaux, E. E., Cady-Pereira, K. E., and Gaustad, K. L.: Retrieving liquid water path and precipitable water vapor from the Atmospheric Radiation Measurement (ARM) microwave radiometers, IEEE Trans. Geosci. Remote Sens., 45, 3680–3690, https://doi.org/10.1109/TGRS.2007.903703, 2007.

Van Zandt, T. E.: A brief history of the development of wind-profiling or MST radars, Ann. Geophys., 18, 740–749, https://doi.org/10.1007/s00585-000-0220-1, 2000.

Velden, C., Daniels, J., Stettner, D., Santek, D., Key, J., Dunion, J., Holmlund, K., Dengel, G., Bresky, W., and Menzel, P.: Recent innovations in deriving tropospheric winds from meteorological satellites, Bull. Amer. Meteor. Soc., 86, 205–224, https://doi.org/10.1175/BAMS-86-2-205, 2005.

Walbröl, A., Crewell, S., Engelmann, R., Orlandi, E., Griesche, H., Radenz, M., Hofer, J., Althausen, D., Maturilli, M., and Ebell, K.: Atmospheric temperature, water vapour and liquid water path from two microwave radiometers during MOSAiC, Scientific Data, 9, 534, https://doi.org/10.1038/s41597-022-01504-1, 2022.

Wang, W., Lei, H. C., Wang, Z. Y., Guo, X. J., and Nie, H. H.: Identification of radio-frequency interference in brightness-temperature data from an airborne microwave radiometer, Plateau Meteor., 37, 1033–1041 (in Chinese), https://doi.org/10.7522/j.issn.1000-0534.2017.00084, 2018.

Wen, J., Su, Z., Wang, X., Zheng, D., Lv, S., Zeng, Y., Liu, R., Zhang, T., and Wang, Z.: Progress in brightness-temperature simulation and soil-moisture retrieval using a ground-based L-band radiometer (ELBARA-III), Plateau Meteor., 40, 1337–1346 (in Chinese), https://doi.org/10.7522/j.issn.1000-0534.2021.zk011, 2021.

Westwater, E. R.: Ground-based microwave remote sensing of meteorological variables, Atmospheric Remote Sensing by Microwave Radiometry, M. A. Janssen, Ed., John Wiley & Sons, 145–213, 1993.

World Meteorological Organization: Guide to Instruments and Methods of Observation, WMO-No. 8, World Meteorological Organization, Geneva, 2021.

Xi, J. J., Zhao, S. Q., Wang, M. S., Jiang, J. X., and Wang, X.: Based on a relative frost factor algorithm retrieving landscape freeze/thaw state by ground-based L-band radiometer, Advances in Geosciences, 10, 437–446 (in Chinese), https://doi.org/10.12677/AG.2020.105039, 2020.

Xia, H., Chen, Y., Yuan, J., Su, L., Yuan, Z., Huang, S., and Zhao, D.: Windshear detection in rain using a 30-km-radius coherent Doppler wind lidar at a mega airport on the plateau, Remote Sens., 16, 924, https://doi.org/10.3390/rs16050924, 2024.

Xu, G. R., Wang, X. F., Wan, R., Li, P., Li, Y. S., and Wang, J. C.: Observed macro- and microphysical characteristics of summer nonprecipitating clouds in Jiulong on the eastern Tibetan Plateau, Torrential Rain Disasters, 43, 135–145 (in Chinese), 2024.

Xu, G. R., Zhang, W. G., Wan, X., Wang, B., Leng, L., Zhou, L. L., and Wan, R.: Atmospheric temperature and humidity profiles retrieved by a ground-based microwave radiometer at Ganzi on the eastern Tibetan Plateau, Torrential Rain Disasters, 38, 238–248 (in Chinese), https://doi.org/10.3969/j.issn.1004-9045.2019.03.006, 2019.

Yang, H., Li, H. L., Wang, B., Zhang, W. G., and Cui, C. G.: Summer precipitation variability over the Three-River Source and river-bend regions and its response to the Plateau summer monsoon, Chinese J. Atmos. Sci., 47, 881–892 (in Chinese), 2023.

https://doi.org/10.5194/egusphere-2026-5310
Preprint. Discussion started: 9 September 2026

Zeng, Z., Wu, H., Liu, Z., Zhao, L., Liang, Z., Liang, Z., and Wang, Y.: Enhancing short-term wind speed prediction capability of numerical weather prediction through machine learning methods, J. Geophys. Res. Atmos., 129, e2024JD041822, https://doi.org/10.1029/2024JD041822, 2024.

Zhao, Y., Kang, Z., Sun, W., Zhang, L., Zhu, K., Wen, H., Zeng, Z., Yang, J., Zhang, D., and Ding, M.: Accuracy assessment of ground-based microwave radiometer in the Mount Qomolangma region, Atmos. Res., 306, 107450, https://doi.org/10.1016/j.atmosres.2024.107450, 2024.